Practical Applications of Hot-Isostatic Pressing Diagrams: Four Case Studies

E. ARZT, M. F. ASHBY, and K. E. EASTERLING

The construction of mechanism maps for hot-isostatic pressing is described. Maps are constructed for a number of materials of commercial and scientific interest: a tool steel, a superalloy, Al_2O_3, and ice. They allow the processes involved in hot-isostatic pressing to be examined, and suggest ways of picking optimum combinations of pressure, temperature, and time to give maximum density.

I. INTRODUCTION

SEVERAL mechanisms contribute to densification during hot-isostatic pressing (HIP). When a pressure is applied to packed powder particles, it is transmitted through the powder bed as a set of forces acting across the particle contacts. The deformation at these contacts is at first *elastic*, but as the pressure rises, the contact forces increase, causing *plastic yielding* and expanding the points of contact into contact areas. Once these contact areas can support the forces without further yielding, time-dependent deformation processes determine the rate of further densification: those we consider are *power-law creep* in the contact zones and *diffusion* from a grain-boundary source to the void surface. The contributions of other possible nondensifying processes, such as vapor transport, are usually insignificant because they are not enhanced by an applied pressure.

All of these processes enlarge both the area and the number of the contacts between particles so that the contact force per unit area (the *effective pressure*) diminishes. This can change the dominant mechanism, which depends not only on the external variables (applied pressure p and temperature T) but also on the current effective pressure—and thus the current geometry.

The overall behavior is complicated because each densifying mechanism has a different dependence on particle size $2R$, on the external variables p and T, and on powder properties and current geometry. One way of analyzing it is to construct *hot-isostatic pressing diagrams* or *HIP maps* which identify the dominant mechanism and predict densification rates and times, as a function of pressure and temperature. Those presented here are based on models for the individual mechanisms of hot-pressing. They show promising agreement with the very limited experimental data. Their use as a guide for analyzing or designing HIP processes and as a tool for analyzing a natural HIP process (the densification of ice in glaciers) is illustrated by four case studies. The next three sections describe the models and the construction of HIP maps. The reader interested in applications may wish to turn directly to Section V.

E. ARZT, formerly Research Assistant, Engineering Department, University of Cambridge, is now Research Scientist at the Max-Planck-Institut für Metallforschung, Stuttgart, West Germany; M. F. ASHBY is Professor of Engineering, University of Cambridge, Engineering Department, Trumpington Street, Cambridge CB2 1PZ, England; and K. E. EASTERLING is Professor of Materials Engineering, University of Luleå, Department of Engineering Materials, S-951 87 Luleå, Sweden.

Manuscript submitted February 11, 1982.

The symbols used, with their units, are listed at the end of Section V.

II. GEOMETRY OF THE MODEL

A. *The Initial Stage*

The model used in our calculations contains two stages. During the *initial stage* (relative density $D < 0.9$), the contacts between the initially-spherical particles (radius R) grow in size and in number; throughout, the deformation is localized in and near the contact regions. The pores are cusp-shaped, and the individual particles and their contact regions can still be distinguished. Densification is determined by the deformation of the particle contacts.

During this stage, the powder is assumed to consist of spherical particles of a single size. If rearrangement of powder particles is disregarded—and cold compaction experiments[1] show that this mechanism is operative only at the very beginning of compaction—then the arrangement of particle centers can be characterized throughout densification by a radial distribution function. We chose that of a random dense packing of equal spheres.[2] Certain geometric parameters can then be calculated. Since the calculations are lengthy, we will quote the results here; details can be found elsewhere.[3,4]

The densification process is modeled by allowing each spherical particle to increase in radius around fixed centers. If the initial particle radius is R, the new particle radius is given by:

$$R' = (D/D_0)^{1/3}R \qquad [1]$$

D is the relative density, D_0 the initial relative density (for random dense packing, $D_0 = 0.64$). The densification rate $\dot{D}$ and the linear shrinkage rate $\dot{y}$ (the rate of approach of neighboring particle centers) are related:

$$\dot{D} = 3(D^2D_0)^{1/3}\dot{y}/R \qquad [2]$$

As the spheres grow, new particle contacts are created so that their current number Z is:

$$Z = Z_0 + C\left(\frac{R'}{R} - 1\right) \qquad [3]$$

where $Z_0 = 7.3$ is the initial number of contacts per particle and $C = 15.5$ is the slope of the radial density function of a random dense packing in the range of interest.

ISSN 0360-2133/83/0211-0211$00.75/0
© 1983 AMERICAN SOCIETY FOR METALS AND THE METALLURGICAL SOCIETY OF AIME

Neighboring spheres now overlap. The volume that has to be removed from the contact zones by any one of the densifying mechanisms is given by:[3]

$$V = \frac{\pi}{R'^3}\left[\frac{1}{3}Z_0(R' - R)^2(2R' + R) + \frac{C}{12R}(R' - R)^3(3R' + R)\right]$$

The derivative of this volume with respect to time gives the excess volume per second associated with densification (see Eq. [19]). If it is assumed that this material is deposited evenly across the free (noncontacting) surfaces of each sphere, then the total contact area on the surface of one particle can be approximated by:

$$a \cdot Z = R^2\frac{(D - D_0)}{D}[160(D - D_0) + 16] \qquad [4]$$

and the neck radius by:

$$x = (D - D_0)^{1/2}R \qquad [5]$$

It can be shown further[3] that in a random packing the external pressure p produces an average contact force f:

$$f = \frac{4\pi R^2}{ZD}p \qquad [6]$$

Hence the *effective pressure* on any particle contact during stage 1 (including surface tension as an additional driving force and the effect of gas trapped in the pores) is:

$$p_1^* = \frac{4\pi R^2 p}{aZD} + p_s - p_i \qquad [7]$$

where

$$p_s = \gamma\left(\frac{1}{\rho} - \frac{1}{x}\right),\ \rho = \frac{x^2}{2(R - x)} \qquad [8]$$

and

$$p_i = p_o\frac{(1 - D_c)D}{(1 - D)D_c}$$

where p_o is the outgassing pressure and D_c is the density at which the pores close.

B. *The Final Stage*

During the *final stage* ($D > 0.90$), the compact is modeled as a homogeneous solid containing spherical voids, such that pores of equal size remain at each vertex of a tetrakaidecahedral particle (a good approximation for the particle shape at high compact densities). Then the pore radius is:[5]

$$r = R\left(\frac{1 - D}{6}\right)^{1/3} \qquad [9]$$

the effective pressure is simply:

$$p_2^* = p + \frac{2\gamma}{r} - p_i \qquad [10]$$

where r is given by Eq. [9] and p_i by Eq. [8].

III. MECHANISMS OF DENSIFICATION

A. *Densification by Rate-Independent Plasticity*

While the pressure is sufficient to cause plastic flow in the compact, densification is instantaneous; it ceases when the contact areas have grown to a size such that the yield stress is no longer exceeded. For the *initial stage* we adopt as a yield criterion the indentation solution:

$$\frac{f}{a} = 3\sigma_y \qquad [11]$$

Using Eq. [6], we find the limiting external pressure required to cause yielding in Stage 1:

$$p_{\text{lim}} = \frac{3\sigma_y}{4\pi R^2}aZd \qquad (D \leq 0.9) \qquad [12]$$

where aZ is given explicitly by Eq. [4].

It is rare that the compact enters the *final stage* during plastic flow. It will do so only if the pressure is high enough to cause the yielding of a spherical shell surrounding each void,[6] requiring that:

$$p_{\text{lim}} = \frac{2\sigma_y}{3} \cdot \ln\left(\frac{1}{1 - D}\right) \qquad (D > 0.9) \qquad [13]$$

In computing densification maps, we compare the rates of competing mechanisms (to determine which is dominant) and sum the rates of independent mechanisms (to obtain the overall rate of densification). To do so, we describe this mechanism by the rate equation:

$$\dot{D} = \infty \quad \text{if} \quad p > p_{\text{lim}}$$
$$\dot{D} = 0 \quad \text{if} \quad p \leq p_{lim} \qquad [14]$$

B. *Densification by Power-Law Creep*

When yielding stops, the contact regions continue to deform by power-law creep. An exact solution for the power-law creep taking place at the contact faces during the *initial stage* is difficult, but the following dimensional argument gives a useful approximate solution.

A circular punch with section πx^2 (the particle contact area) indents a power-law creeping solid (the particle), for which:

$$\bar{\dot{\varepsilon}} = \dot{\varepsilon}_0\left(\frac{\bar{\sigma}}{\sigma_0}\right)^n \qquad [15]$$

where $\bar{\dot{\varepsilon}}$ and $\bar{\sigma}$ are the equivalent (von Mises) strain rate and stress, respectively, and $\dot{\varepsilon}_0$, σ_0, and n are material properties. If the effective pressure over the contact face is p_1^*, then the stresses in the material below the punch must scale as p_1^*, so that

$$\bar{\sigma} = C_1 p_1^*$$

The displacement rate of the punch must scale as the strain rate $\bar{\dot{\varepsilon}}$ and as the radius x of the contact zone, which is the only length which enters the problem, giving $\dot{y} = C_2\bar{\dot{\varepsilon}}\,x$. Stresses and strains are related by the constitutive law (Eq. [15]), so that:

$$\dot{y} = C_2\dot{\varepsilon}_0 x\left(\frac{C_1 p_1^*}{\sigma_0}\right)^n$$

But we require that, in the limit $n = \infty$ and $\sigma_0 = \sigma_y$ this reduces to the perfectly plastic solution to the problem (Eq. [11]); then $C_1 = \frac{1}{3}$. Further, we require that, in the elastic limit $n = 1$, $\dot{\varepsilon} \equiv \varepsilon$, and $\sigma_0/\dot{\varepsilon}_0 \equiv E$ (where E is the Young's modulus), we recover the Hertz solution for the indentation displacement y of two elastic spheres;[7] this it does if $C_2 = 9\pi/16$. The result is:

$$\dot{y} = \frac{9\pi}{16} x \dot{\varepsilon}_0 \left\{\frac{p_1^*}{3\sigma_0}\right\}^n$$

Using Eq. [2] the rate of densification is:

$$\dot{D} = 5.3(D^2 D_0)^{1/3} \frac{x}{R} \dot{\varepsilon}_0 \left(\frac{p_1^*}{3\sigma_0}\right)^n \qquad [16]$$

where the neck radius x is defined in Eq. [5] and the effective pressure p_1^* in Eq. [7].

During the *final stage*, densification is determined by the creep of the thick spherical shell surrounding each hole.[8,9] The exact solution for this case is:

$$\dot{D} = \frac{3}{2} \dot{\varepsilon}_0 \frac{D(1-D)}{[1-(1-D)^{1/n}]^n} \left(\frac{3}{2n} \frac{p_2^*}{\sigma_0}\right)^n \qquad [17]$$

where p_2^* is given by Eq. [10].

C. *Densification by Diffusion*

Matter may be transported from the contact zones to the surface of a sintering neck by both grain-boundary and lattice diffusion. This mechanism is important in pressureless sintering and is enhanced in hot-isostatic pressing by the compressive traction acting on the grain boundary between the particles.

During the *initial stage*, the volume of the material deposited on the surface of the sintering necks of one particle by boundary diffusion per second is given by:[9]

$$\dot{V} = \frac{4\pi(\delta D_b + \rho D_v)}{kT} \Omega Z p_1^* \qquad [18]$$

where ρ is given by Eq. [8], or (in terms of D) by Eqs. [5] and [8]. Here δD_b is the boundary diffusion coefficient times its thickness, D_v is the lattice diffusion coefficient, Ω is the volume of the diffusing atom or molecule, and k is Boltzmann's constant. If this is set equal to the excess volume caused by an increment of densification (see Section II), we obtain:

$$\dot{D} = \frac{12D^2}{D_0 R^3 g(D)} \frac{(\delta D_b + \rho D_v)}{kT} \Omega Z p_1^* \qquad [19]$$

where $g(D)$ is a purely geometric term:

$$g(D) = \left[\left(\frac{D}{D_0}\right)^{2/3} - 1\right]\left\{Z_0 + \frac{c}{4}\left[\left(\frac{D}{D_0}\right)^{2/3} - 1\right]\right\}$$

The effective pressure p_1^* is given by Eq. [7] and Z by Eq. [3].

This result combines the diffusion kinetics for one contact with the increase in coordination during densification. It should be emphasized that for this mechanism it is not the total contact area $a \cdot Z$ which determines the rate of densification, but rather the average area of a single contact: many small contacts densify faster than a few large ones, and for this reason also, the rate of the diffusional mechanism depends strongly on particle size R, whereas that of power-law creep is independent of R.

During the *final stage*, matter is transported along the grain boundaries onto the surfaces of spherical grain-boundary voids. The solution for this case is:[9]

$$\dot{D} = 54 \frac{\Omega(\delta D_b + rD_v)}{kTR^3} \cdot \left\{\frac{[1-(1-D)^{2/3}]}{3(1-D)^{2/3} - [1+(1-D)^{2/3}]\ln(1-D) - 3}\right\} p_2^* \qquad [20]$$

D. *Other Considerations*

The mechanisms described above, as far as we know, account for densification during hot-isostatic pressing; in this sense, the treatment of this paper is a complete one. But their rates can be influenced by factors which have been ignored in deriving the rate equations.

The most important is probably grain growth. When pressing is rapid there is little time for grain growth; but when the compact is held for an hour or more at around two-thirds of its melting point (as it is in a typical HIP cycle), grain growth may remove the grain boundary from many of the necks between powder particles. This has no influence on plasticity or power-law creep, but it suppresses diffusional densification. We do not yet know how to model grain growth during hot-pressing properly, but once an adequate model is available it can be easily incorporated into the computational scheme for the maps.

A second omission is the influence of surface diffusion or vapor transport in maintaining a pore shape which is close to the equilibrium one. This problem has been analyzed for pressureless sintering,[5] where it is shown that, if surface redistribution within the pore is slow, the rate of sintering can be limited, not by diffusion along the path that removes matter from the boundary to the pore (as is normally assumed), but by the rate at which subsequent redistribution takes place within the pore. A similar condition can arise during pressure sintering, retarding diffusional densification, but leaving densification by the other two mechanisms unaffected. Its importance, at present, is unknown.

IV. CONSTRUCTION OF THE MAPS

We have constructed three kinds of maps: one for a fixed pressure, with axes of density D and homologous temperature T/T_M; the second for a fixed temperature, with density D and normalized pressure $p/\sigma_y(T)$ as variables; and the third for a given density with p and T as axes. Examples are shown in Figures 1, 3, and 6.

The maps are constructed by evaluating the rate equations at sets of values of D, p/σ_y, or T/T_M which form a closely spaced grid in the chosen axis set. The dominant mechanism is identified as that which gives the greatest densification rate. Field boundaries (heavy lines) bound a field in which one mechanism (power-law creep or diffusion) is dominant; and at a field boundary, two mechanisms contribute equally to densification. At high densities, the internal gas pressure eventually becomes equal to the densifying pressure (the external pressure p plus the pressure due to the

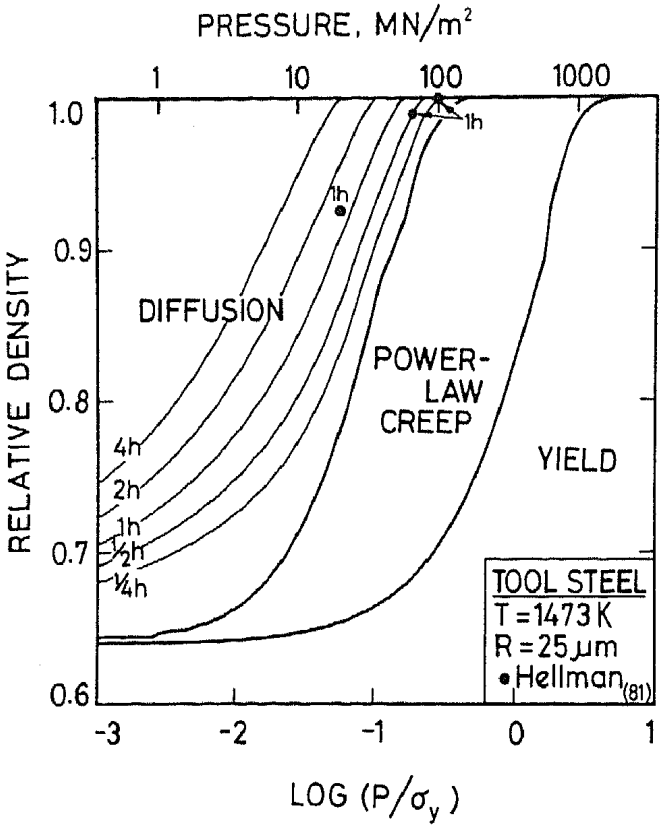

Fig. 1—A density/pressure map at T = 1473 K for tool steel with a particle diameter of 50 μm.

surface tension, γ/ρ or $2\gamma/r$). This field, marked "NO DENSIFICATION", is shown on the map for ice (Figure 13). We disregard the effect of entrapped gas for industrial HIP processes, since the powder is usually outgassed before the pressure is applied.

Superimposed on the fields are contours of constant time (thin lines). They are obtained by numerically integrating the rate-equations. Densification rates contributed by each mechanism are added linearly, since all mechanisms are assumed to act independently. The sudden change to the final stage equations at $D = 0.90$ introduces discontinuities in both the contours and the boundaries; these have been smoothened by an averaging algorithm.

The construction of the maps requires data for the material properties which enter the rate equations. Data for the maps shown below are listed in Table I, with explanatory notes. It should be understood that the precision of the maps is neither better nor worse than that of the rate equations and data used to construct them. The individual rate equations have now been tested by direct comparison with carefully controlled laboratory tests (see, for example, Swinkels *et al*[10]) and appear to be accurate to better than a factor of 2. The biggest source of error is usually the uncertainty in material data, particularly those for boundary diffusion and for power-law creep. The powder particle size, too, is often imprecisely known, and in any real process a distribution of sizes exists. We have sometimes found it best to change slightly the particle size, R, used in the calculations to get a good fit to diffusional densification when data are available; the size has no influence on power-law creep. But despite these uncertainties, the success of the case studies (below) in matching industrial data gives some confidence in the predictive power of the method.

V. CASE STUDIES

In this section we compare pressure sintering maps, constructed from the rate-equations of Section III, with data from commercial and natural hot-isostatic pressing processes. These data are inadequate for a complete test of the method, but the comparison is informative and illustrates the predictive power of the maps. In particular, it is worth remembering that where diffusional mechanisms are dominant, the particle size, and grain growth, have a profound influence on densification rate, whereas when power-law creep is dominant, it has no influence at all.

A. *Tool Steels*

The production of high-alloy tool steels is a successful commercial example of hot-isostatic pressing. The method provides a manufacturing route by which large carbide-forming additions are retained in a homogeneous distribution, giving a tool which wears well at high cutting speeds and temperatures. Such tools are increasingly used in manufacturing industry, particularly in heavy-duty operations like broaching and milling. The composition in Table II is typical of tool steels made in this way. Data for the hot-isostatic pressing of tool steels are assembled in Table III.

Maps describing the hot-isostatic pressing of tool steels are shown in Figures 1 to 5. Heavy lines show field boundaries; thinner lines contours of constant time computed from the rate equations. Experimental data are shown as full circles and are labeled with the (experimental) time to reach that density.

Figures 1 and 2 show density/pressure maps at a constant temperature of 1200 °C, for two particle sizes (R = 25 and 50 μm). The data of Hellman[13] are plotted on the map for the smaller particle size: agreement is good. The map shows that the normal hot-pressing conditions of p = 100 MN/m^2 and T = 1200 °C cause densification by power-law creep up to a relative density of about 0.98, but that achieving full density requires diffusion. The particle size can therefore be important in the pressing of tool steels.

The density/temperature maps for p = 100 MPa (Figures 3, 4, and 5) make the same point: the industrial conditions of temperature and pressure (chosen by trial and error) lie almost entirely within the power-law creep field, where the advantages of applying a pressure are greatest (because $\dot{D} \propto p^n$); but the removal of the last 2 pct or so of porosity probably occurs by boundary diffusion.

Note that the pressing temperature is high—only 300 °C below the melting point (about 0.9 T_M). In this case, increasing the pressure (rather than the temperature) may be the best way to achieve full density more rapidly (compare Figures 2 and 5). This point is made in a more forceful way by the pressure/temperature map at a density of 0.99, shown in Figure 6. The two full lines labeled "tool steel" show the trade-off between temperature and pressure, to reach D = 0.99 in one hour.

B. *The Nickel-Based Superalloys*

The superalloys are nickel-rich alloys, strengthened by a solid solution and by a precipitate of γ' ($Ni_3(Ti,Al)$) and of various carbides. Their remarkable high-temperature

Table I. Material Data

Material Property		Al_2O_3 (e)	Tool Steel (f)	Superalloy (g)	Ice (h)
Atomic Volume, Ω (m^2)		4.25×10^{-29}	1.21×10^{-29}	1.1×10^{-29}	3.27×10^{-29}
Burger's Vector, b (m)		4.76×10^{-10}	2.58×10^{-10}	2.5×10^{-10}	4.52×10^{-10}
Melting Temperature, T_M (K)		2320	1680	1673	273.15
Shear Mod. at 300 K, μ_0 (Pa)		1.55×10^{11}	8.1×10^{10}	8.3×10^{10}	2.91×10^{9}
Temperature Dependence, $\frac{T_m}{\mu_0}\frac{d\mu}{dT}$	(a)	−0.35	−0.85	−0.5	−0.35
LATTICE DIFFUSION					
D_{ov}, (m^2/s)	(b)	2.8×10^{-3}	3.7×10^{-5}	1.6×10^{-4}	9.1×10^{-4}
Q_v, (kJ/mole)		477	280	285	59.4
BOUNDARY DIFFUSION					
δD_{ob}, (m^3/s)	(b)	8.6×10^{-10}	2×10^{-13}	2.8×10^{-15}	8.3×10^{-13}
Q_b, (kJ/mole)		419	167	115	38.3
POWER-LAW CREEP					
n		3.0	7.5	4.6	3
A, (Dorn Constant)	(c)	3.38	1.5×10^{12}	1.22×10^{5}	$\sigma_0 = 1 \times 10^6$, $\dot{\varepsilon}_0 = 8.2 \times 10^8 \exp -\frac{Q_{cr}}{RT}$
Q_{crp}, (kJ/mole)		477	280	285	80
YIELD STRENGTH at 0 K, σ_y^0 (Pa)		1.3×10^{10}	9.1×10^{8}	9.05×10^{8}	7.5×10^{7}
$\frac{T_M}{\sigma_y^0}\frac{d\sigma_y}{dT}$	(d)	−1.38	−4.5	−4.5	0
SURFACE ENERGY γ (J/m^2)		≈1	≈1	≈1	0.1

Notes for Table I

(a) A temperature dependent modulus has been used, given by:

$$\mu = \mu_0\left(1 + \frac{(T - 300)}{T_M}\left(\frac{T_M d\mu}{\mu_0 dT}\right)\right)$$

(b) The diffusion coefficients are given by:

$$D_v = D_{ov} \exp -(Q_v/RT)\ m^2/s \quad \text{(lattice diffusion)}$$

$$\delta D_b = \delta D_{ob} \exp -(Q_b/RT)\ m^3/s \quad \text{(boundary diffusion)}$$

(c) The quantities $\dot{\varepsilon}_0$ and σ_0 of Eq. [15] are related to the material properties listed here by:

$$\frac{\dot{\varepsilon}_0}{\sigma_0^n} = \frac{AbD_v}{kT\mu^{n-1}}$$

See Frost and Ashby[11] for a comprehensive tabulation of such data. For ice, σ_0 and $\dot{\varepsilon}_0$ are given.

(d) A temperature dependent yield strength has been used, given by:

$$\sigma_y = \sigma_y^0\left(1 + \frac{T - 300}{T_M}\left(\frac{T_M}{\sigma_y^0}\frac{d\sigma_y}{dT}\right)\right)$$

(e) *Alumina.* The data are for pure alumina, and are largely taken from Frost and Ashby.[11] The surface energy is roughly that cited by Kingery.[12]

(f) *Tool Steel.* There are no creep data for tool steels at HIP temperatures (around 1200 °C). In this temperature range the steel is austenitic and all the alloying elements are in solid solution. The mechanical properties should resemble those of a high alloy steel at the same temperature. Accordingly, we have used mechanical data and diffusion coefficients for 304 stainless steel.[11]

(g) *Nimonics.* There are no creep data for nimonics above the γ'-solvus when the alloy is an fcc solid solution. The best estimate we can make is to use data for a high-chromium Nichrome, for which good data exist.[11]

(h) *Ice.* The data for pure polycrystalline ice are from Frost and Ashby.[11]

strength and resistance to gas corrosion recommend them for discs and blades in gas turbines. Recently the hot-isostatic pressing of powders, either directly to shape, or to a preshape which is then forged, has been developed by a number of manufacturers. The pressing may be carried out either below or above the γ' solvus, depending on whether grain growth is to be avoided or desired. The advantages of the process are the compositional uniformity of the final product, the saving in machining and finishing costs, and potential saving of material. Data for the hot-isostatic pressing of superalloys are collected in Table IV.

Maps for a "typical" superalloy with two different particle sizes are shown in Figures 7 to 10. Data for the industrial

Table II. Composition of Typical HIP-Cutting Tool (Wt Pct)

C	Cr	Mo	W	V	Co
1.3 to 2.3	~4.0	5.0 to 7.0	~6.5	3.1 to 6.5	8.5 to 10.5

Table III. Data for the Hot-Isostatic Pressing of Tool Steel

Mean Diameter (μm)	Pressure (MN m^{-2})	Temperature (°C)	Time (Hours)	Density (Pct)	Source and Comment
~40 (30 to 600)	400	20	4	69 to 74	ASEA[14]
(24 Mesh)	100	1100	2	"full"	Bryck[15] Takigawa[16]
*	40	1100	0.5	"full"	Poor bond strength
	40	1200	0.5	"full"	Good bond strength
*	100	1000	1	0.966	Hellman[13]
		1000	2	0.982	
*		1050	1	0.996	
		1100	1	0.997	
		1100	2	0.998	
		1150	1	0.998	
*	200	1200	1	0.926	
	65		1	0.989	
	100		1	0.999	
	150		1	full	

*not stated

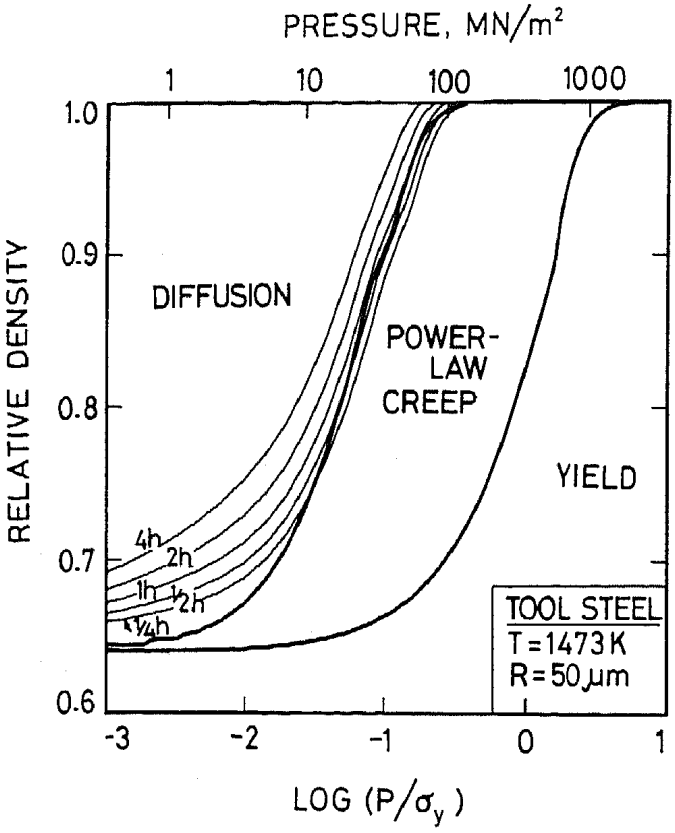

Fig. 2—A density/pressure map at T = 1473 K for tool steel with a particle diameter of 100 μm.

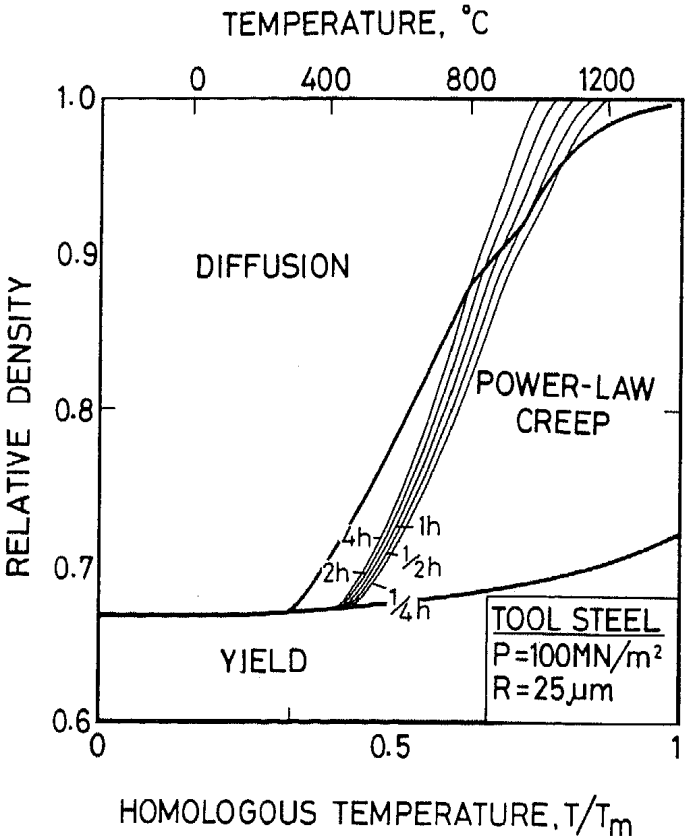

Fig. 3—A density/temperature map at p = 100 MN/m^2 for tool steel with a particle diameter of 50 μm.

processes are plotted on the maps. They relate to conditions which give full density only, and do not allow a critical check of the maps (as the tool-steel data did). The density/pressure maps for 1200 °C (Figures 7 and 8) show that like the tool steels, densification at 100 MPa is mainly by power-law creep, but that diffusion may contribute in an important way to achieving full density. The corresponding density/temperature maps for 100 MPa (Figures 9 and 10), too, confirm this, and illustrate how the use of smaller particles accelerates this final stage of densification.

The trade-off between the pressure and temperature required to give a density of 0.99 in one hour is shown, for both particle sizes, on Figure 6 (broken lines).

C. *Alumina*, Al_2O_3

The relatively high strength and toughness of sintered alumina make it attractive as a structural ceramic. Until recently it has been consolidated by pressureless sintering, using additives (such as MgO) to give a liquid phase which

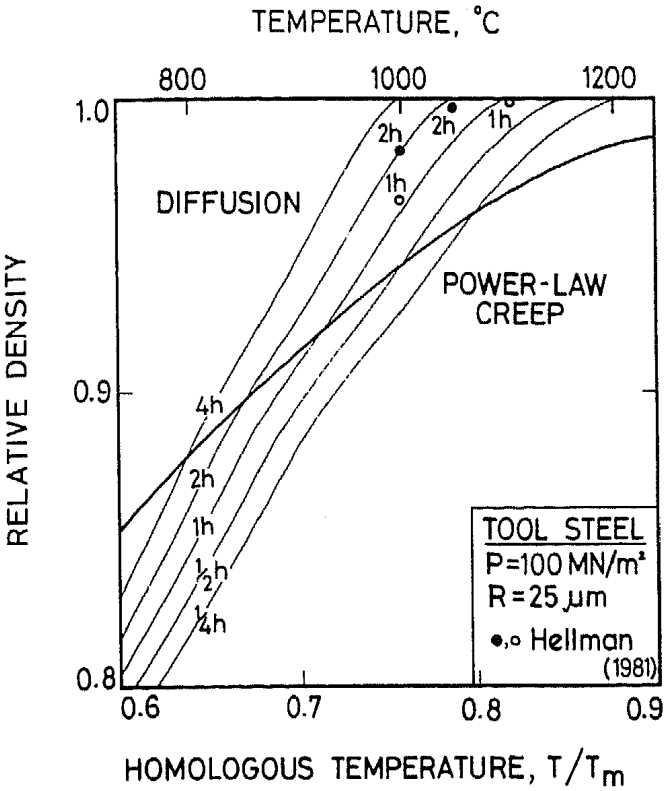

Fig. 4—An enlarged section of the density/temperature map shown in Fig. 3.

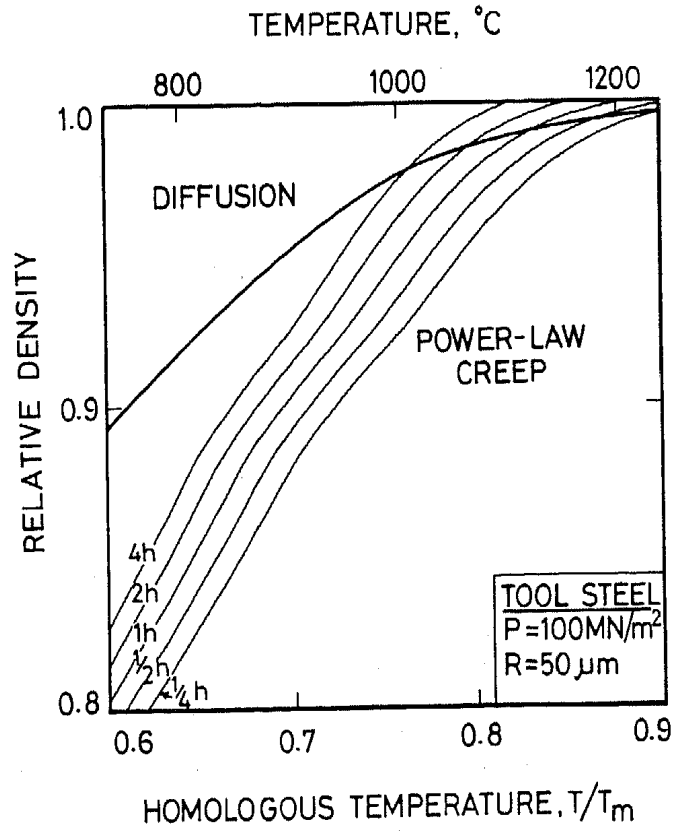

Fig. 5—An enlarged section of a density/temperature map at p = 100 MN/m^2 for tool steel with a particle diameter of 100 μm.

accelerates sintering. But hot-isostatic pressing offers the possibility of achieving high densities without the contaminating effect of additives, a particularly attractive goal when fabricating storage cans for nuclear waste and wear-resistance cutting tools. The most complete hot-isostatic pressing data are those of ASEA,[14] who used high purity

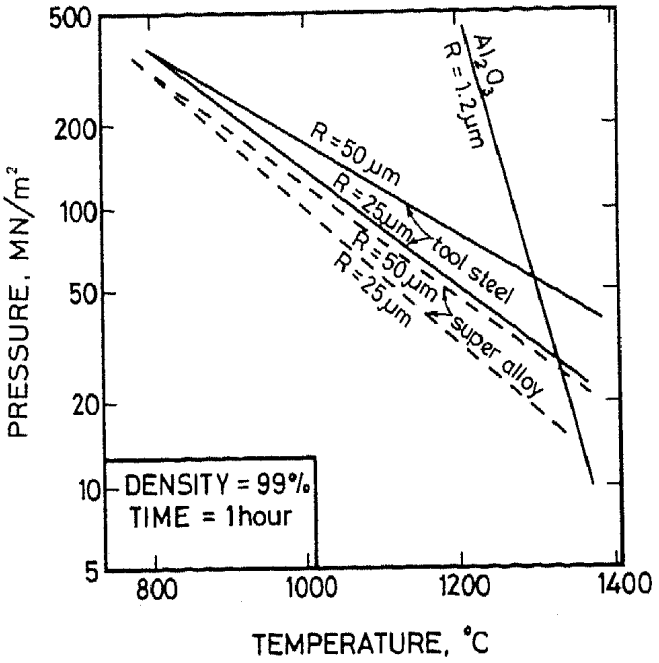

Fig. 6—A pressure/temperature map, showing the combination of p and T required to achieve a relative density of 0.99 in 1 h. It shows the trade-off between pressure and temperature and the influence of particle size on this.

(>99.5 pct) alumina powders. These and other data are summarized in Table V.

Maps for the hot-pressing of alumina with a particle size of 2.5 μm are shown in Figures 11 and 12. The experimental data of ASEA[14] are shown as circles, and are labeled with the experimental time required to reach that density. The density/pressure map for 1200 °C (Figure 11) is in good agreement with the ASEA data, and shows that densification is by grain boundary diffusion throughout densification. The map also shows the extent to which a change in pressure changes densification: an increase in pressure to 200 MN/m^2 (at 1200 °C) gives full density in two hours—an increase to 400 MN/m^2 gives full density in one hour.

A density-temperature map for 100 MPa is shown in Figure 12. It, too, shows good agreement with the industrial data, and illustrates that a small change in temperature (as little as 30 °C) can halve the time required to reach full density.

This point is better illustrated by Figure 6. The full line for Al_2O_3 shows the combinations of pressure and temperature which lead to a density of 0.99 in one hour. The line is much steeper than that for the metals because, in Al_2O_3, diffusion dominates densification. (When the line is steep, increasing temperature is more effective than increasing pressure, and *vice versa*.)

The maps suggest (a) that increasing the temperature rather than the pressure should be the best way to reduce processing times (assuming that times are not already limited by thermal conduction into the compact); and (b) that, since grain boundary diffusion is the dominant mechanism, the particle size is a critical variable: reducing the size greatly accelerates sintering, and procedures which minimize grain growth should maximize the density.

D. *The Pressure Sintering of Polar Glaciers*

In polar regions, ice condenses from the atmosphere and precipitates, often as fine spherical particles. They sinter

Table IV. Data for the Hot-Isostatic Pressing of Superalloys

Mean Diameter (μm)	Pressure (MN m^{-2})	Temperature (°C)	Time (Hours)	Density (Pct)	Source and Comments
60 (argon atomized)	100	1140	4	full	Aubin *et al*[17] Astroloy
450 (by rotating electrode)	100	1170	4	full	
*	140	1170	4	full	Lamberigts *et al*[18]
35 mesh	180	996	1	full	Gessinger and Bomford[19], IN 100
35 mesh	180	1260	1	full + grain growth	
50 (150 max.)	70 to 100	1100 to 1220	2	full in 20 minutes	Rolls Royce[27]
≈60	100	1200	3	full	Evans and Judd[20] Low-C Astroloy
150	40	1100	4	full	Mitkov[21]
150	40	1150	2	full	Powder APK 1
≈40	100	1107	3	full; grain size = 22 μm	Podob[22]
	100	1213	3	full; grain size = 45 μm	

*not stated

Table V. Data for the Hot-Isostatic Pressing of Alumina

Mean Diameter (μm)	Pressure (MN m^{-2})	Temperature (°C)	Time (Hours)	Density (Pct)	Source and Comments
2.5	150	1350	2	full	ASEA[14]
2.5	100	1200	2	97.5	
2.5	100	1200	4	98.1	Green density =
2.5	200	1200	2	99.6	60 to 65 pct
2.5	200	1200	4	99.5	Estimated density at
2.5	100	1300	2	99.6	HIP temperature = 70 pct
2.5	100	1300	4	99.6	
2.5	200	1300	2	99.5	Cold isostatic pressing
2.5	100	1400	2	99.7	at 100 MPa used to
2.5	100	1400	4	99.7	obtain 65 pct density.
2.5	200	1400	2	99.8	
2.5	200	1400	2	99.6	
0.5	150	1350	2	full	ASEA.[14] Extreme grain growth.
*	69 to 138	1150 to 1370	0.5 to 3	"full"	Morgen and Sands[23]
*	103	1410	*	*	Irving[24]

*not stated

under the combined driving forces of surface tension and the pressure due to the weight of the particles deposited on top of them. Data are available from two widely separated sites: Byrd Station in Antarctica[25] and Site 2 in Greenland.[26] Both lie in the dry snow zone, where no melting occurs during the summer, and both are on parts of an ice field which undergoes very little shear. At both sites the temperature, density, and age of the ice have been measured as a function of depth (Table VI).

The top few meters of the compacted ice are very porous, and within this zone the temperature fluctuates with the seasons. But below 20 m, where the relative density of the ice is greater than 0.7, the individual ice particles can no longer be distinguished, the pores are cylindrical or spherical, and the temperature stabilizes to a constant, season-independent value of −27 °C (0.9 T_M). From 20 m to 400 m the pressure rises almost linearly with depth and the ice increases in relative density to a limiting value of 0.997.

In constructing maps, it seemed more realistic — in view of the low packing density of ice — to set $D_0 = 0.5$. The average contact area was calculated as $a = x^2\pi(1 - 0.64)/(1 - D_0)$, with x from Eq. [5] (this is the simplest correction which approaches Eq. [5] at high densities, but gives a finite value of a at $D = 0.64$). The coordination number was obtained from Eq. [3], with $D_0 = 0.5$.

A density/pressure map for ice at −27 °C is shown in Figure 13. It shows a large field of power-law creep, and a field labeled "NO DENSIFICATION" in which the internal pressure of the air trapped in the pores, initially 0.1 MPa, equals the pressure due to the overburden of ice. It is a general feature of hot-isostatic pressing that densification rates for both power-law creep and diffusion diminish to zero at the boundary with the field of "NO DENSIFICATION," and diffusion always takes over as the terminal mechanisms.

The densities predicted by the map agree well with those observed and plotted on the figure. The dominant mechanism of densification of polar ice is power-law creep, not diffusion. The end-point density at 400 m is predicted to be 0.995, very close to that observed in the field. Grain growth is observed at depths above about 100 m, but this has little

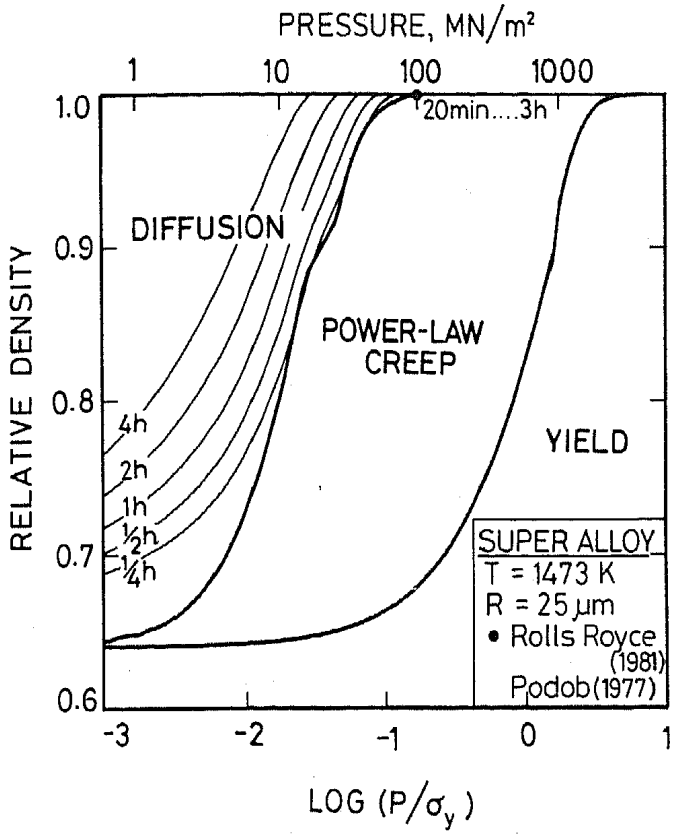

Fig. 7—A density/pressure map at T = 1473 K for a superalloy with a particle diameter of 50 μm. Data point represents industrial conditions (Table IV).

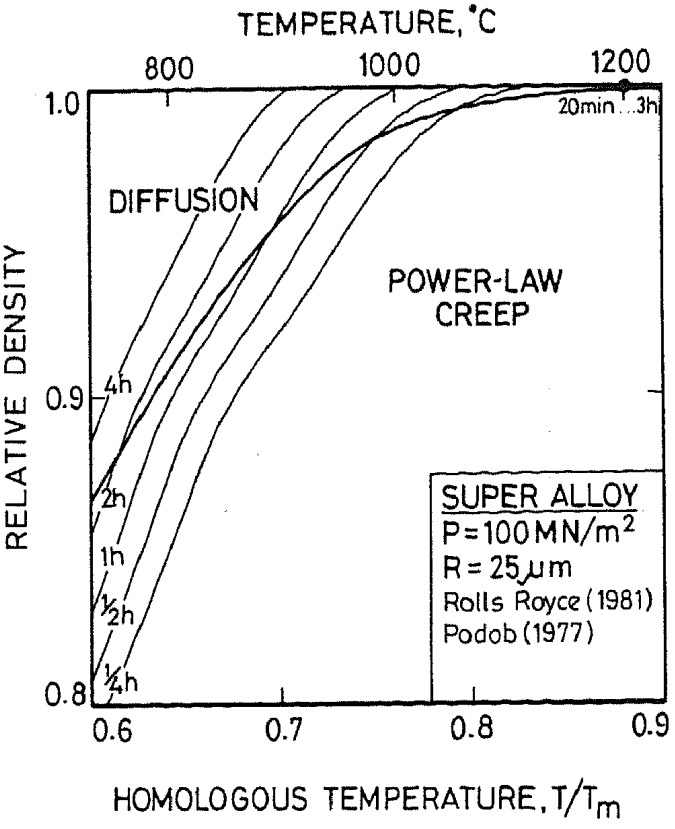

Fig. 9—A density/temperature map at p = 100 MN/m² for a superalloy with a particle diameter of 50 μm.

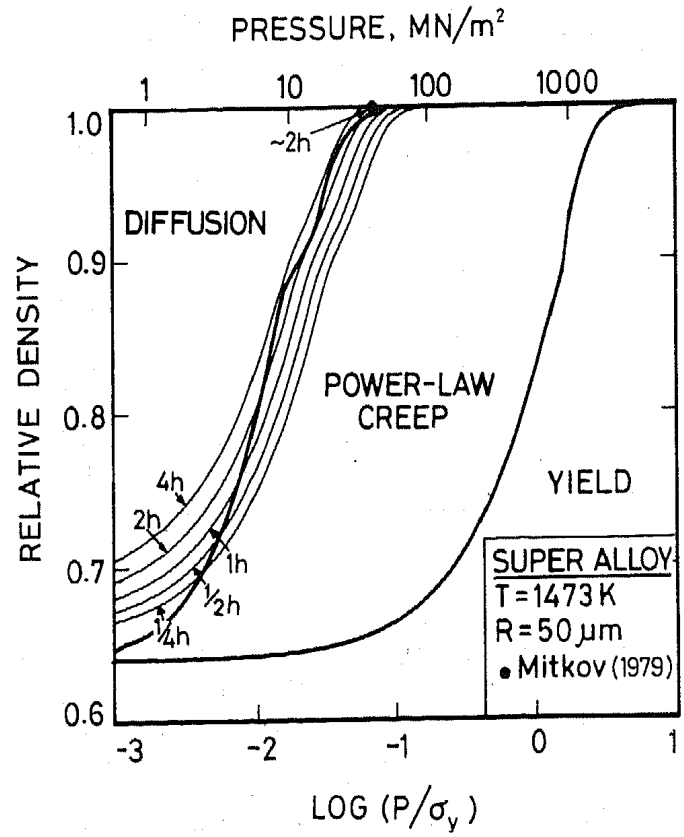

Fig. 8—A density/pressure map at T = 1473 K for a superalloy with a particle diameter of 100 μm.

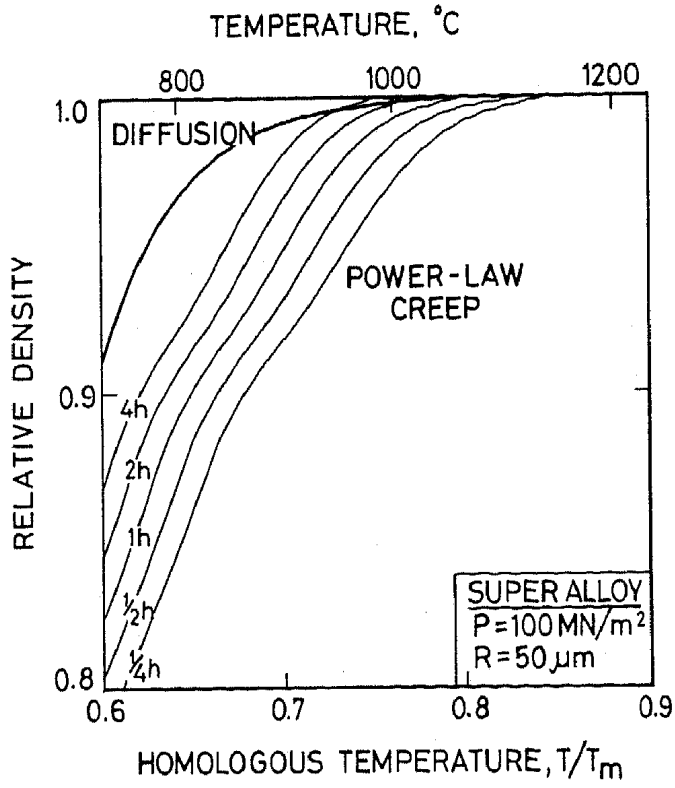

Fig. 10—A density/temperature map at p = 100 MN/m² for a superalloy with a particle diameter of 100 μm.

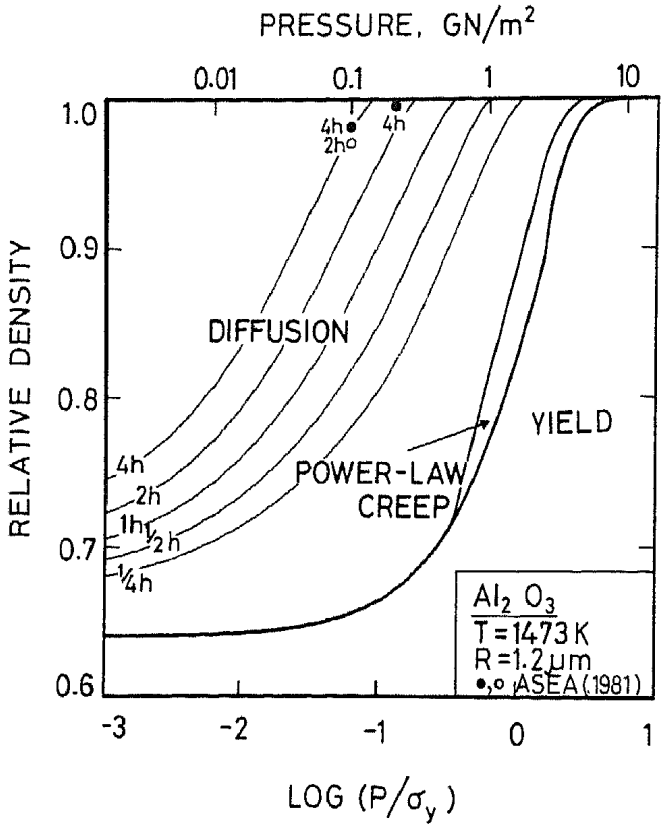

Fig. 11—A density/pressure map at $T = 1473$ K for alumina with a particle diameter of 2.5 μm.

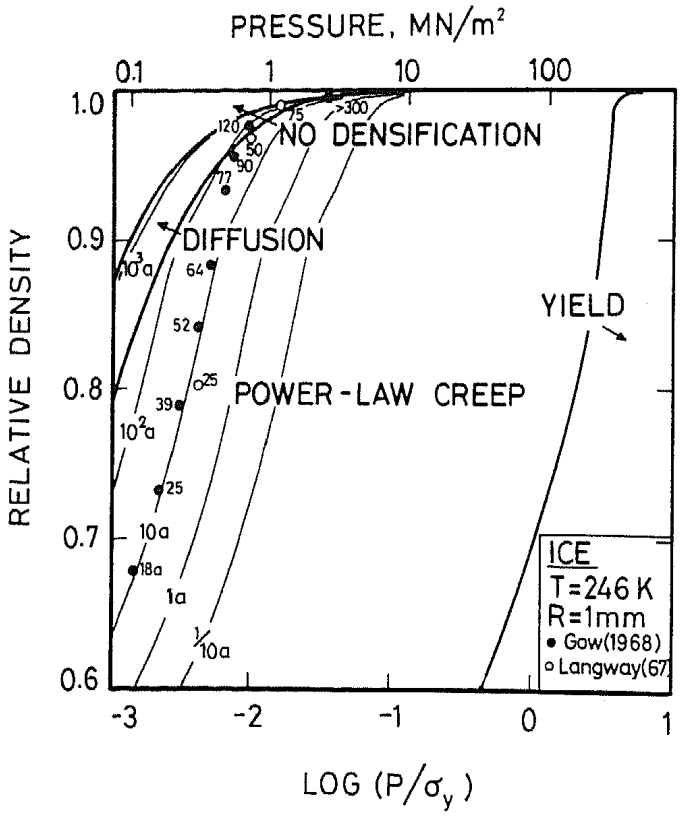

Fig. 13—A density/pressure map at $T = 246$ K for ice with a particle diameter of 2 mm.

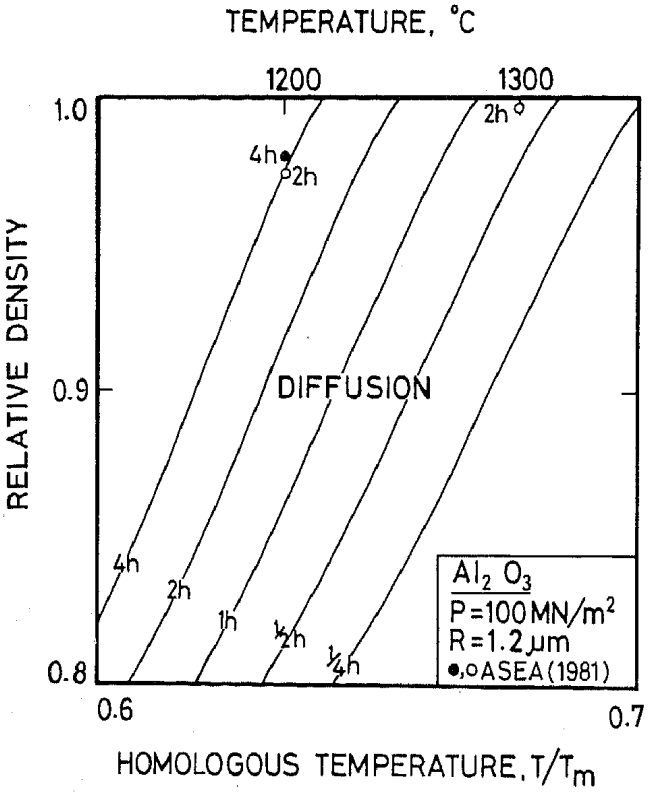

Fig. 12—A density/temperature map at $p = 100$ MN/m² for alumina with a particle diameter of 2.5 μm.

Table VI. Data for the Densification of Ice

Site and Reference	Depth (m)	Pressure (MPa)	Age* (Years)	Relative Density
Site 2, Greenland[26]	50	0.32	25	0.804
	100	0.75	50	0.971
	150	1.19	75	0.991
	400	3.63	250	0.997
Byrd Station, Antarctica[25]	20	0.11	18	0.679
	30	0.17	28	0.733
	40	0.24	39	0.789
	50	0.32	52	0.843
	60	0.40	64	0.885
	70	0.49	77	0.934
	80	0.58	90	0.957
	100	0.76	120	0.978
	300	2.62	>300	0.995

*Age roughly corrected for continuous loading up to pressure cited (actual age/$(n + 1)$, where $n = 3$ is the power-law creep exponent of ice).

effect on the density because it does not influence the rate of power-law creep. The map shown in Figure 13 uses a particle size of 2 mm, the smallest likely to be found in polar ice—since larger particles suppress diffusional mechanisms even further, the conclusion that polar ice densifies by power-law creep seems to be a general one.

If the data for ice are trustworthy (as they appear to be), the method outlined here could be used to predict the density profiles in other, unstudied, ice bodies.

SYMBOLS AND UNITS

p	External pressure (MN m^{-2})
T	Temperature (K)
f	Average contact force (N)
p_1^*, p_2^*	Effective pressure for stage 1 (average contact force/average contact area) and stage 2 (MN m^{-2})
p_i	Pressure of internally trapped gas (MN m^{-2})
p_s	Pressure due to surface tension (MN m^{-2})
p_o	Atmospheric (or outgassing) pressure (MN m^{-2})
D	Relative density
D_0	Relative density at start of pressing (taken as 0.64)
D_c	Relative density at which pores close
$\dot{D}$	Densification rate (s^{-1})
x	Neck radius (m)
$\dot{x}$	Neck growth rate (m s^{-1})
$2y$	Center-to-center particle spacing (m)
$2\dot{y}$	Rate of approach of particle centers (m s^{-1})
R	Particle radius (m)
r	Pore radius during final stage sintering (m)
ρ	Radius of curvature of neck (m)
Z	Average number of contact neighbors per particle
a	Average area of one particle contact (m^2)
σ_y	Yield strength of particle material (MN m^{-2})
$\dot{\varepsilon}_0, \sigma_0, n$	Power-law creep parameters (s^{-1}, MN m^{-2}, $-$)
δD_b	Grain-boundary diffusion coefficient times boundary thickness (m^3 s^{-1})
D_v	Lattice diffusion coefficient (m^2 s^{-1})
Ω	Atomic volume (m^3)
γ	Surface energy (J m^{-2})
C	Slope of radial distribution function for particle packing (for dense random packing $C = 15.5$)

ACKNOWLEDGMENT

We wish to acknowledge the support of the S.E.R.C. through a Senior Visiting Fellowship and a Research Grant.

REFERENCES

1. H. Fischmeister, E. Arzt, and L. Olsson: *Powder Metall.*, 1978, vol. 21, pp. 179-87.
2. G. Scott: *Nature*, 1962, vol. 194, pp. 956-58.
3. H. Fischmeister and E. Arzt: *Powder Metall.*, in press.
4. E. Arzt: *Acta Metall.*, 1982, vol. 30, pp. 1883-90.
5. F.B. Swinkels and M.F. Ashby: *Acta Metall.*, 1981, vol. 29, pp. 259-81.
6. G. Torre: *Berg-u. Hüttenm. Mh.*, 1948, vol. 93, pp. 62-78.
7. S.P. Timoshenko and J.N. Goodier: *Theory of Elasticity*, McGraw-Hill, New York, NY, 1970, p. 409.
8. D.S. Wilkinson and M.F. Ashby: *Acta Metall.*, 1975, vol. 23, pp. 1277-85.
9. D.S. Wilkinson: Ph.D. Thesis, University of Cambridge, 1977.
10. F.B. Swinkels, D.S. Wilkinson, E. Arzt, and M.F. Ashby: Cambridge University, Report CUED/C/MATS/TR73, 1981.
11. H.J. Frost and M.F. Ashby: *Deformation Mechanism Maps*, Pergamon Press, Oxford, 1982.
12. W.D. Kingery: *Introduction to Ceramics*, Wiley, New York, NY, 1960, p. 194.
13. P. Hellman: Uddeholm A.B., Sweden, private communication, 1981.
14. H. Larker: ASEA, Robertsfors, Sweden, private communication, 1981.
15. D. Bryck: Proc. Powder Metall. Conference, Grenoble, 1974.
16. H. Takigawa, H. Manto, N. Kawai, and K. Homma: *Powder Metall.*, 1981, vol. 24, pp. 196-202.
17. C. Aubin, J.H. Davidson, and J.P. Trottier: in *Superalloys 1980*, J.K. Tien, S.T. Wlodek, H. Morrow, M. Gell, and G.E. Maurer, eds., American Society for Metals, Metals Park, OH, 1980, pp. 345-54.
18. M. Lamberigts, E. Diderrich, D. Coutsouradis, E. de Lamotte, and J.M. Drapier: in *Superalloys 1980*, *ibid.*, pp. 285-94.
19. G.H. Gessinger and M.J. Bomford: *Intern. Met. Rev.*, 1974, vol. 19, pp. 51-76.
20. D.J. Evans and G.M. Judd: *Modern Developments in Powder Metallurgy*, H.H. Hausner and P.V. Taubenblat, eds., Metal Powder Industries Federation, Princeton, NJ, 1976, vol. 10, pp. 199-210.
21. M. Mitkov: in *Sintering Processes*, G.C. Kuczynski, ed., Plenum Press, New York, NY, 1979, vol. 13, pp. 505-15.
22. M.T. Podob: in *Modern Developments in Powder Metallurgy*, H.H. Hausner and P.V. Taubenblat, eds., Metal Powder Industries Federation, Princeton, NJ, 1977, vol. 11, pp. 25-44.
23. W.R. Morgan and R.L. Sands: *Met. Rev.*, 1969, vol. 14, p. 85.
24. R.R. Irving: *Iron Age*, 1963, vol. 10, pp. 17-22.
25. A.J. Gow: Report RR197, United States Army Cold Regions Research and Engineering Laboratory, 1968.
26. C.C. Langway, Jr.: Report RR77, United States Army Cold Regions Research and Engineering Laboratory, 1967.
27. Rolls-Royce: private communication, 1981.